Materials Advances

ROYAL SOCIETY OF CHEMISTRY

PAPER

View Article Online
View Journal | View Issue

Cite this: *Mater. Adv.*, 2025, 6, 9655

The efficiency of an aminated nanocrystalline cellulose stabilized binary Ag–ZnO nanocomposite as an electrode platform for electrochemical sensing of ascorbic acid

Md. Mahabur Rahman,[ab] Md. Sohel Rana,[a] Hideto Minami,[c] Md. Mahbubor Rahman,[a] Md. Abdur Rahman,[a] Md. Ashraful Alam[a] and Hasan Ahmad *[a]

This work details the fabrication of a graphite coated aminated nanocrystalline cellulose stabilized Ag–ZnO nanocomposite electrode for application in electrochemical sensing and quantification of ascorbic acid (AA) in biological samples. The prepared nanocomposite is named ANCC/Ag–ZnO, where ANCC stands for aminated nanocrystalline cellulose. The graphite coated ANCC/Ag–ZnO electrode produced a high electrochemical response because of binary Ag–ZnO nanoparticles and the stability, high surface area, porosity, and crystallinity of nanocellulose. The ANCC particles are prepared by amination of nanocrystalline cellulose (NCC), with the latter being synthesized from raw rice (*Oryza sativa*) straw. The green ethanol extract from mussaenda flower (*M. erythrophylla*) bracts is used as a reducing agent to generate Ag–ZnO nanoparticles. The average diameter of a spherical ANCC/Ag–ZnO nanocomposite is around 9.77 nm. The graphite coated ANCC/Ag–ZnO nanocomposite electrode demonstrated an 8 times increase in cyclic voltammogram (CV) current response compared to the native graphite coated ANCC electrode. The electrocatalytic oxidation of AA showed a good linearity over a wider range of 0–16.0 mM with a regression value of 0.9934. The sensitivity and limit of detection (LOD) are 0.543 mA mM^{-1} cm^{-2} and 0.031 mM, respectively, and the electrode possessed a good reproducibility (RSD, 2.06%). The nanocomposite electrode retained about 81% of its initial current response after 1500 cycles. The synthesized ANCC/Ag–ZnO nanocomposite material is found to be applicable for electrochemical sensing and quantification of AA in biological samples without overlapping signals from other interfering agents.

Received 11th June 2025,
Accepted 16th October 2025

DOI: 10.1039/d5ma00624d

rsc.li/materials-advances

Introduction

In contemporary scientific society, a growing number of researchers are becoming interested in developing electrode platforms based on nanomaterials for precise and accurate detection and quantification of analytes (*e.g.*, pollutants, biomolecules, active drug molecules, *etc.*) in a sample. Electrochemical sensing is widely recognized as a powerful analytical technique that converts small chemical changes at the electrode to a measurable electrical signal and offers advantages of high sensitivity, quick response, cost economy, *in situ* monitoring capacity, good reproducibility, specificity, easy process, *etc.* over traditional methods.[1–10]

The direct use of bare electrodes like Pt, Au, Ag, glassy carbon and graphite in electrochemical sensing results in nonspecific adsorption or fouling at the electrode interface, poor sensitivity and detection, high overpotential and a slow redox process.[3,11–13] Modification of electrodes with metal (Ag, Cu, Pd, Pt, and Au) and metal oxide (Fe_3O_4, MnO_2, SnO_2, ZnO, TiO_2, and NiO) nanoparticles is one promising avenue for rapid and accurate electrochemical detection because of their higher electron transfer kinetics, reduced overpotential, unique electrocatalytic and electronic properties, large surface area, and variable morphology and size.[14–21] Recently, the binary and ternary metal/metal oxide nanocomposites as electrode modifiers in electrochemical sensors have attracted increasing interest as they contribute individual properties of each metal, synergistic effects from interactive cooperation, and improved electrocatalytic and electron transfer kinetics.[11,22] However, research in the area of mixed metal–metal oxide nanocomposites in electrochemical sensing is still limited. For example, an iron functionalized ZnO nanocomposite (FeZnO) synthesized

[a] *Research Laboratory of Polymer Colloids and Nanomaterials, Department of Chemistry, Rajshahi University, Rajshahi 6205, Bangladesh. E-mail: samarhass@yahoo.com, hahmad@ru.ac.bd; Tel: +88 01716389382*
[b] *Department of Chemistry, Pabna University of Science and Technology, 6600 Pabna, Bangladesh*
[c] *Graduate School of Engineering, Kobe University, Kobe 657-8501, Japan*

by a hydrothermal method has been evaluated for sensing monosodium glutamate and nitrite, showing good accuracy, selectivity and stability.[23] An rGO stabilized binary Cu–iron oxide-based nanocomposite on a 3D printed Ag-electrode (Fe–Cu–rGO@Ag) showed high selectivity and linear response towards electrochemical detection of blood creatinine.[24] Maduraiveeran *et al.* observed a low limit of detection (LOD), high sensitivity and good selectivity for a flower-like NiO@Au nanocomposite as a lactic acid sensor.[25] Ponnaiah *et al.* devised a uric acid sensor using polyaniline coupled Ag–Fe_2O_3 nanostructures with improved electrical conductivity.[26] Abdel-Hameed *et al.* synthesized Ag/ZnO nanorods *via* a coprecipitation method and modified the carbon paste electrode for roxadustat detection and validated its use in analyzing pharmaceutical formulations and human plasma.[27] Vijayalakshmi *et al.* prepared an Ag–ZnO nanocomposite by halium, a green extract, mediated co-precipitation and modified the graphite electrode for Cu ion quantification in ferrocyanide solution.[28] The other mixed metal–metal oxides included $NiCo_2O_4$, Fe_3O_4@MnO_2 and rGO–polydopamine–$ZnMnO_3$ hybrid materials for electrochemical detection.[29–31]

In a previous investigation, we prepared aminated nanocrystalline cellulose (ANCC) stabilized binary Ag–ZnO (ANCC/Ag–ZnO) nanocomposite particles as a less toxic antimicrobial platform.[32] The amination of nanocrystalline cellulose derived from raw rice (*Oryza sativa*) straw and subsequent binding with Ag–ZnO nanoparticles reduced the cytotoxicity, which is beneficial for safe applications in textile, medical, and health-related products. The amination of NCC introduced reactive amine groups (–NH_2) on the cellulose surface, which coordinated strongly with Ag^+ and Zn^{2+} ions, thus promoting higher nucleation density and nanoparticle loading compared to unmodified NCC.[32] The amine groups also improved nanoparticle dispersion by imparting electrostatic stabilization and steric hindrance, which effectively reduced agglomeration. As a result, ANCC acted not only as a stabilizing matrix but also as an active participant in nanoparticle anchoring, leading to enhanced stability, uniformity, and a larger electroactive surface area. This chemical fixation of metal–metal oxide nanoparticles also made them stable to washing and air oxidation. In a green approach, the alcoholic extract of mussaenda flower (*Mussaenda erythrophylla*) bracts was used during *in situ* co-reduction of Ag and Zn ions to generate hybrid Ag–ZnO nanoparticles. The aerial part of the *Mussaenda* genus generally contains large amounts of phenolic compounds along with steroids, tetraterpene, flavonol and derivatives of quinic acid.[33] In order to justify the application versatility, here, an attempt is made to apply a graphite-modified antimicrobial ANCC/Ag–ZnO nanocomposite for electrochemical sensing/detection of ascorbic acid (AA). The incorporation of Ag^+ into the hybrid structure will improve the electrocatalytic efficiency and accelerate the active oxidation.[28] The large specific surface area and porous structure of ANCC should favor the sorption and diffusion of analytes to the active detective sites, which ultimately should produce enhanced sensitivity, accuracy, and response rates.[34] Despite the expected advantages, exploration of the above literature suggests that neither the ANCC nor the NCC as a support material for mixed metal–metal oxide nanoparticles has been emphasized in electrochemical analysis. Even the work on the ANCC/NCC stabilized monometallic platform in electrochemical sensing is scarcely available. In the present investigation, it is therefore hypothesized that chemical binding of binary Ag–ZnO nanoparticles to porous ANCC of high specific surface area would produce an excellently stable new biosensing material with improved sorption and diffusion capacity of analytes. Additionally, the ANCC as a biocompatible material would facilitate *in vivo* applications of the resultant nanocomposite in contact with blood in the fields of biosensing, drug delivery, bioimaging, bone regeneration, anti-inflammatory materials, wound dressing, and tissue engineering.[34–36] Here, AA was chosen as an analyte considering its importance as a human nutrient and wider presence in pharmaceutical products, cosmetics, foods (peppers, brussels sprouts, tomatoes, broccoli, potatoes, citrus fruits, and cauliflower), and food products. AA plays a vital role as a neurochemical agent in the brain, participates in many biochemical processes as a cofactor for enzymes, and supports biosynthesis, cell metabolism of carnitine, iron absorption in intestine, wound healing, amino acid metabolism, *etc.*[37,38] AA is also a potent antioxidant that can prevent free-radical induced diseases.[39] The shortage of AA can cause some common illnesses like respiratory infections, cold, inability to achieve pregnancy, anemia, cancer, hypertension, mental insanity, failure of neurotransmitters, weakness, fatigue, rheumatoid arthritis, and Parkinson's and Alzheimer's diseases.[40,41] Excess AA in the body can also cause bladder stones, diarrhea, and gastric irritation.[39] Therefore, accurate determination of AA in biological fluids is important for evaluating the actual cause of disease and health disorders. There are many methods for AA measurement, and all of those are time-consuming, costly, and require skilled manpower.[42,43] Consequently, the present work deals with the electrochemical estimation of AA using a graphite modified ANCC/Ag–ZnO nanocomposite electrode, and the performance is compared with each ANCC and bare Ag–ZnO modified graphite electrode. The ANCC/Ag–ZnO nanocomposite modified graphite electrode demonstrated excellent sensitivity and robust stability. Detection of AA in human serum as a real sample is also achieved.

Experimental section

Materials

Raw straw of rice (BRRI 28: *O. sativa*) from a nearby agricultural field (Bangladesh) was used as a source of ANCC. Toluene (99.9%), acetic acid (99.9%), HCl (37%), and *N*,*N*-dimethyl formamide (DMF, 99.8%) were procured from Merck, India. NaOH (98%) and H_2SO_4 (96%), purchased from Merck, Germany were used for cellulose recovery and hydrolysis. $NaClO_2$ (Loba Chemie, India, 80%) and ethanol (Changshu Hongsheng, China, 99.9%) were used as received. *p*-Toluene sulfonyl chloride (TsCl, >98%) from Sigma Aldrich, Germany was used for

NCC activation. Ag–ZnO nanoparticles were prepared from $AgNO_3$ (Active Fine Chem., Bangladesh, 99.8%) and $Zn(CH_3COO)_2{\cdot}2H_2O$ (QualiKems, India, 98%) precursor salts. Triethylamine hydrazinium hydroxide (TEA, 99%) and diethylamine (DEA) were procured from Thomas Baker, India. All chemicals, LiCl (99%), Na_2CO_3 (99.9%), and $NaHCO_3$ (99%) from QualiKems, India were stored in the desiccator before use. *N*,*N*-Dimethyl acetamide (DMAc, 99.5%) was purchased from Nice Chemicals, India and used as received. A graphite rod collected from a commercially available sunlight high super multipurpose UM-1 (R-20 D) 1.5 V battery was used as the working electrode for electrochemical investigations. *N*-Methyl-2-pyrrolidone (NMP) was obtained from Sigma-Aldrich Chemie GmbH (USA). Deionized distilled (DD) water was used for cleaning purposes and sample preparation, which was collected from a reverse osmosis and UV purification system (Puricom, Taiwan).

Preparation of aminated nanocrystalline cellulose (ANCC)

The preparation of ANCC particles was carried out according to the literature.[32] In brief, 15.0 g of washed rice straw (*O. sativa*) powder was dewaxed by stirring (500 rpm) for 24 h in a 2 : 1 (v/v) toluene/ethanol mixture. The dewaxed powder was recovered and dried. 13.0 g of dewaxed powder was then treated with 300 mL of 5% NaOH solution at 30 and 90 °C for 24 and 2 h, respectively, to drive off fats, hemicellulose, pectin, and remaining wax. The resultant white cellulose powder was repeatedly washed with DD water until the pH value was neutralized and then dried under room conditions. Finally, bleaching was carried out using 500 mL of 1.4% (w/v) acidic (pH ∼ 4.0) $NaClO_2$ solution at 70 °C for 5 h. The product was filtered, washed, and dried, and the yield of the ultimate bleached pulp was 37.4% (w/w).

1.0 g of bleached pulp was magnetically stirred (700 rpm) with 15 mL of 60% (v/v) H_2SO_4 in a 25 mL Erlenmeyer flask at 25 °C for 25 min. The brown suspension turned milky white following the addition of 200 mL of ice water. The suspension was dialyzed with DD water until the suspension turned almost neutral and then dried under vacuum to obtain NCC powder (yield 35.6% w/w).

A two-step process was implemented for the amination of NCC to obtain ANCC.[32,44] NCC powder (0.5 g) was stirred (750 rpm) with 1.0 g of LiCl in 13 mL of DMAc at 100 °C for 30 min, followed by another 24 h at 25–30 °C. The off-white-colored suspension of NCC was mixed with 2 mL of TEA (basic) in 1.0 mL of DMAc and magnetically stirred (750 rpm) for 30 min. The temperature was reduced to below 5 °C, 3.5 g of TsCl in 3 mL of DMAc was added dropwise, and the stirring was continued for 6 h. The temperature was raised to 25–30 °C, and the mixing was continued for another 18 h. Then the mixture was poured into 250 mL of ice-water, and the resultant white precipitate of tosylated-NCC was successively washed with DD water and ethanol before drying under vacuum at ambient temperature. Secondly, the tosylated NCC (yield: 72.5%) particles were aminated (ANCC) by treatment with DEA. For this, 0.5 g of tosylated-NCC was allowed to disperse in 5 mL of DMF, and 3 mL of DEA was added slowly at 25–30 °C, while the stirring (500 rpm) was continued for 2 h. Then, the reaction mixture taken in a 100 mL round flask was subjected to reflux at 80 °C for 24 h. The light orange-red color solution of the 6-deoxy cellulose amine derivative was cooled to 25–30 °C before pouring into 100 mL of ethanol. The obtained precipitate was recovered by centrifugation (12 300*g*) and washed with ethanol. The yield of ANCC in the second step was nearly 80.4% (w/w).

Preparation of Ag–ZnO nanoparticles

A 100 mL solution of $AgNO_3$ (0.01 M) was mixed with 100 mL of $Zn(CH_3COO)_2{\cdot}2H_2O$ (0.01 M) in a 250 mL Erlenmeyer flask and stirred magnetically at ∼500 rpm for 10 min. Separately, 30 mL of ethanol extract was adjusted to pH ∼ 7.0 using 0.1 M NaOH. This extract solution was added dropwise to the precursor salt

Fig. 1 Scheme for the preparation of ANCC/Ag–ZnO nanocomposite particles.

solution under continuous stirring (~500 rpm). The reaction pH was maintained between 7.0 and 8.0 with 0.1 M NaOH, and stirring was continued at 60 °C for 6 h. The dark brown Ag–ZnO nanoparticles were collected by centrifugation at 12 300*g*, washed three times with DD water followed by ethanol, and dried under vacuum at 30 °C. The nanoparticles were stored in the dark at 4 °C.

Preparation of the ANCC/Ag–ZnO nanocomposite

The ANCC/Ag–ZnO nanocomposite particles were prepared according to the method illustrated in the literature.[32] Shortly, ANCC (0.35 g) particles dispersed in 130 mL of DD water were mixed with $AgNO_3$ (0.1104 g) and $Zn(CH_3COO)_2{\cdot}2H_2O$ (0.1420 g) in a 250 mL Erlenmeyer flask. 20 mL of ethanol extract (TPC: 2.01 g GAE) from mussaenda flower (*M. erythrophylla*) bracts was added and the pH was adjusted roughly at 7.0–8.0. The reaction mixture was magnetically agitated and the co-reduction of metal ions was continued at 25–30 °C for 6 h. The resultant brown ANCC/Ag–ZnO nanocomposite was recovered by centrifugation and washed three times with DD water and ethanol before drying under vacuum. The complete scheme for the preparation of the ANCC/Ag–ZnO nanocomposite from rice straw is depicted in Fig. 1.

Characterization

The changes in the chemical structure of the prepared samples were followed by Fourier transform infrared (FTIR) spectroscopy (PerkinElmer, FTIR-100, USA). The washed and dried sample was mixed with KBr powder (1 : 4), pressed into pellets and then scanned over the wavelength range of 4000–200 cm^{-1}. The morphology and size distribution were analyzed using a scanning electron microscope, SEM (JSM-6510, JEOL, Tokyo, Japan), and a transmission electron microscope, TEM (JEM-1230, JEOL, Tokyo, Japan), operated at operated at 20 and 100 kV respectively. The elemental composition was followed by recording EDX spectra on an energy dispersive X-ray spectrometer coupled to a field emission SEM (JSM-IT800-IS, Tokyo, Japan) instrument, operating at 15 kV. The phase transitions and metal constituents were identified for powdered samples using an X-ray diffractometer (Bruker D8 Advance, Germany).

Electroanalytical measurements

Electrochemical studies, including cyclic voltammetry (CV) and electrochemical impedance spectroscopy (EIS), were conducted using a Corrtest CS350 electrochemical workstation (China) in a three-electrode system. The graphite rod coated nanocomposite was used as the working electrode, whereas the platinum wire and Ag/AgCl electrode were used as counter and reference electrodes, respectively. Electrode performance was examined in 5.0 mM $[Fe(CN)_6]^{3-/4-}$ with the pH value being adjusted at 7.0 using phosphate buffer solution. All the electrochemical measurements were carried out at 25 °C. The working electrode was fabricated by coating the active part of the graphite rod with a uniform slurry of the prepared material and PVdF binder in a 90 : 10 weight ratio, with NMP as a solvent. The active material coated on the electrode surface was calculated to be 1.8 to 2.0 mg for every fabricated electrode. Coated electrodes were dried in an electric oven at 60 °C for 12 h. Prior to each CV measurement, nitrogen gas was bubbled through the electrolyte for 10 min to remove dissolved oxygen. The working electrode was then placed in the phosphate buffered 5.0 mM $[Fe(CN)_6]^{3-/4-}$ solution and the CV was scanned over a potential window of −0.2 V to +0.6 V at different scan rates (20, 40, 50, and 100 mV s^{-1}). EIS measurements were performed over a frequency range of 5×10^{-2} to 5×10^{-5} Hz with a scan rate of 50 mV s^{-1}. Square-wave voltammetry (SWV) measurements were also conducted using the same three-electrode system in the phosphate buffer solution (pH = 7.0) to evaluate the effect of different scan rates (10 to 100 mV s^{-1}) and a calibration curve was constructed in the potential range of −0.2 to +0.6 V (*vs.* Ag/AgCl).

Results and discussion

Characterization of electrode materials

The chemical structure and functionalization of NCC particles were analyzed by FTIR spectral analysis. The stepwise transformation of raw rice straw to NCC following alkali treatment, bleaching and acid hydrolysis is previously confirmed by FTIR spectral analysis.[32] Here, we focused only on stepwise structural changes during chemical transformations of NCC to ANCC and then to the ANCC/Ag–ZnO nanocomposite. The FTIR spectrum of NCC (Fig. 2a) shows no characteristic vibration signals from the aromatic skeletal structure (C=C) of lignin and the ester linkage of lignin, generally observed at 1515 cm^{-1} and 1730 cm^{-1}.[45–47] Hence, the successive treatments with 5% NaOH, 1.4% (w/v) acidic $NaClO_2$ and 60% (v/v) H_2SO_4 almost completely removed hemicellulose and lignin. The absorption signal at 1640 cm^{-1} represents the bending vibration of –OH from absorbed water. The bands in the range of 1320–1430 cm^{-1} correspond to the CH_2 scissoring, bending and rocking vibrations of cellulose.[32] The stretching bands of the anti-symmetrical pyranose ring skeletal vibration of C–O–C and symmetrical stretching vibration of C–O–C of β-glycosidic linkage appear in the range 895–1160 cm^{-1}.[48] In the spectrum of ANCC (Fig. 2b), a new prominent absorption peak due to –N–H bending at 1568 cm^{-1} confirms the successful amination of the $–CH_2OH$ group by DEA *via* tosylation reaction.[49] Following co-ordination of metal ions with electron rich nitrogen in the –NH– group of aminated cellulose, a slight red shift of –NH– bending occurred from 1568 to 1560 cm^{-1} in the spectrum of the ANCC/Ag–ZnO nanocomposite (Fig. 2d).[50] The stretching bands for Zn–O–Zn, Zn–O–Ag and metal–oxygen bonds in the nanocomposite (Fig. 2d) appear at 1024, 665 and 467 cm^{-1} respectively, also validating the formation of the nanocomposite and matching well with the spectrum of binary Ag–ZnO hybrid nanoparticles (Fig. 2c).

The SEM image of NCC particles in Fig. 3a shows that many tiny perhaps roughly spherical particles (indicated by an arrow) are aggregated. The strong hydrogen bonding interaction among cellulose nanocrystals possibly favored the formation of aggregated networks.[51] It is also probable that sample drying

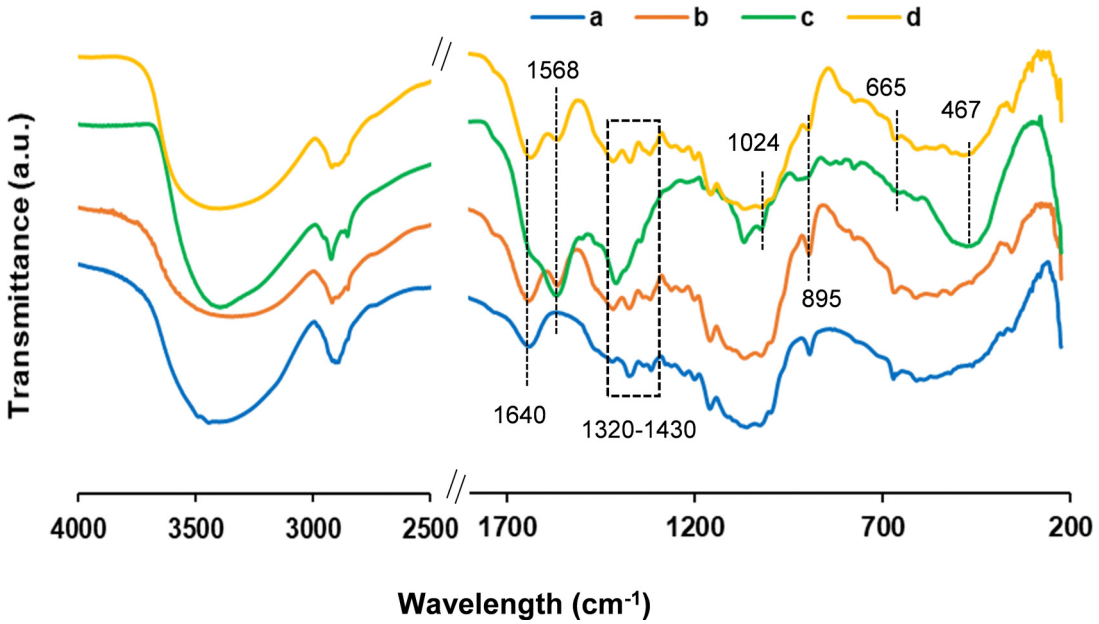

Fig. 2 FTIR spectra of NCC particles (a), ANCC particles (b), the Ag–ZnO hybrid (c) and ANCC/Ag–ZnO nanocomposite (d) particles taken in KBr pellets.

and close packing of cellulose crystallites promoted aggregation *via* hydrogen bond formation.[50] The SEM image of ANCC particles shown in Fig. 3b does not illustrate any difference in the aggregation phenomenon. The SEM micrograph of Ag–ZnO (Fig. 3c) reveals partial agglomeration of roughly spherical nanoparticles. The average size measured using ImageJ software is estimated to be around 223 nm. Comparatively, the SEM image of ANCC/Ag–ZnO nanocomposite particles (Fig. 3d) demonstrates a bit different morphology. Close analysis suggests that large flocs resulted from agglomeration of many tiny nanocomposite particles (the inset of Fig. 3d). The strong hydrogen bonding interaction among ANCC phases prompted such agglomeration. The controlled nucleation, growth and stabilization of Ag–ZnO nanoparticles apparently reduced their average size to a few nanometers. Nevertheless, the coordination of –NH– functionalities of ANCC with Ag^{+} and Zn^{2+} ions during the synthesis process prevented the uncontrolled growth. The EDX spectral analysis of the ANCC/Ag–ZnO nanocomposite displayed in Fig. 3e illustrates the existence of C (43.9 at%), O (51.8 at%), Ag (2.6 at%) and Zn (0.17 at%); possibly Si (1.64 at%) is derived from sample wafer. The nitrogen atom derived from the amine functionality in ANCC

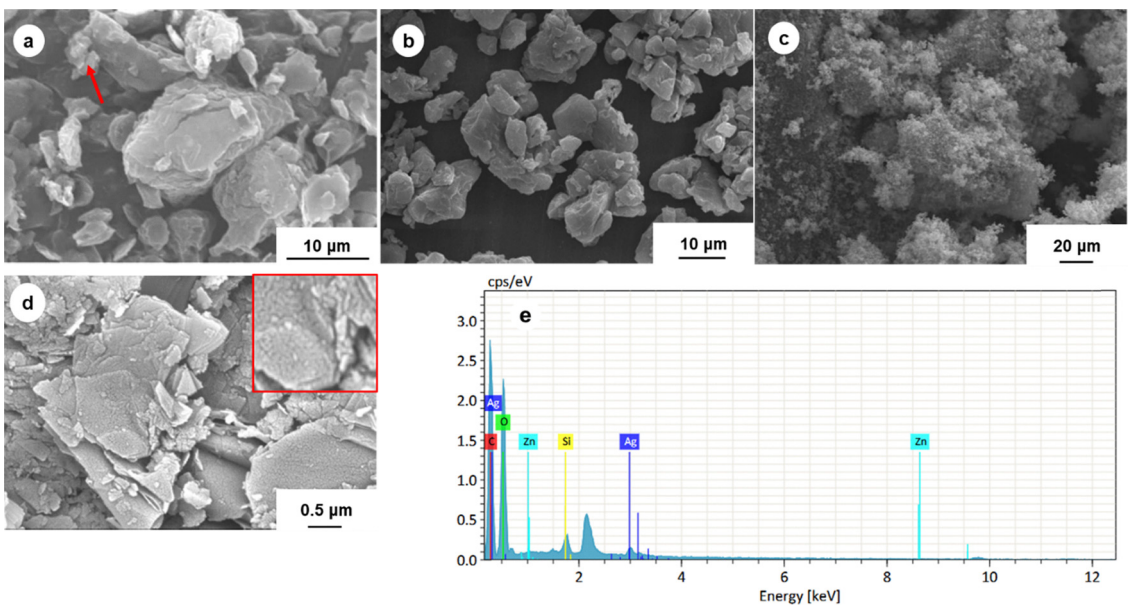

Fig. 3 SEM images (a)–(d) and EDX spectra (e) of NCC (a), ANCC (b), Ag–ZnO (c) and ANCC/Ag–ZnO nanocomposite (d) and (e) particles.

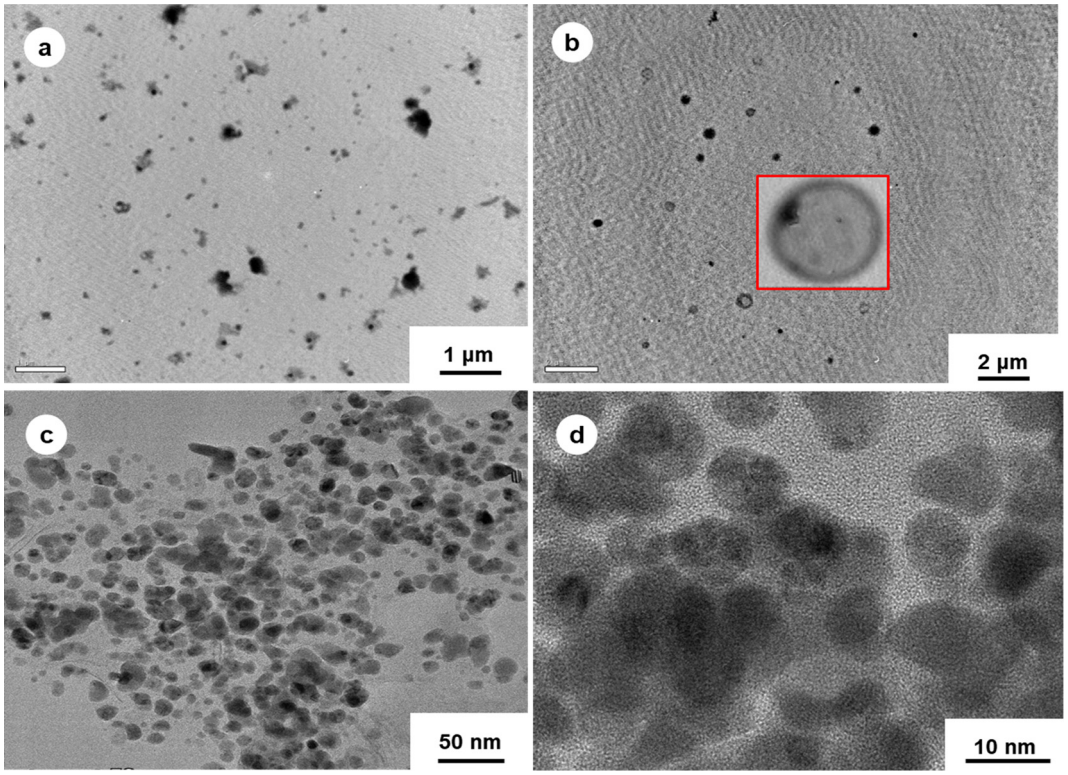

Fig. 4 TEM images of NCC (a), ANCC (b), Ag–ZnO (c) and ANCC/Ag–ZnO nanocomposite (d) particles.

is 10 at% (spectra not shown). But nanocomposite formation and interaction of the electron rich –NH– group with Ag and Zn ions through co-ordination possibly hindered the detection of nitrogen.

In contrast, the TEM images of both NCC (Fig. 4a) and ANCC (Fig. 4b) show the presence of individual particles. It is reasonable to conclude that the soft aggregates are fragmented into individual particles or smaller flocs under a strong electron beam.[48] In either case, particles are mostly spherical, but the presence of elongated particles cannot be ruled out. The average diameter of sphere-shaped NCC particles is calculated to be approximately 147 nm and that of ANCC particles is approximately 300 nm. The larger diameter of ANCC particles is possibly due to the swelling and aggregation, and perhaps the lumen structure formed during sample drying (see the inset image of Fig. 4b). It is obvious that acid hydrolysis and disintegration of the amorphous segment within the cellulose Iβ structure produced such smaller particles. Fig. 4c displays the morphology of bare Ag–ZnO nanoparticles, which are relatively polydisperse and dense due to the electron rich domain. They are independently distributed with the average size being around 13.47 nm. This average size measured from the TEM image is much lower than that measured from the SEM image (Fig. 3d) and perhaps partial aggregation in the latter affected the measurement. The strong electron beam during TEM observation possibly segregated the soft aggregates into individual nanoparticles. In contrast, the ANCC/Ag–ZnO nanocomposite shown in Fig. 4d seems to be more uniformly distributed and less aggregated. The appearance of the nanocomposite indicates the possibility of partial deformation of the cellulose segment adhered to hybrid Ag–ZnO nanoparticles. The lighter part of the nanocomposite belongs to organic ANCC, and the darker part represents the electron-rich Ag–ZnO nanoparticles. The average size of the nanocomposite is 9.77 nm as determined using the ImageJ software. It is reasonable to predict that the stable nano-size distribution results from the coordination of Ag^{+} and Zn^{2+} to cellulose chains through electron-rich –NH–, –OH, and C–O–C groups, proceeded by co-reduction and finally the growth of Ag–ZnO nanoparticles.[52]

The existence of different phases and the formation of multicomponent ANCC/Ag–ZnO nanocomposites were further assessed from XRD analysis. The XRD pattern of hybrid Ag–ZnO nanoparticles illustrated in Fig. 5a demonstrates diffraction signals at 2θ values of 38.2, 44.2, 64.6, and 77.6° corresponding to 111, 200, 220, and 311 lattice planes (JCPDS card no. 04-0783). This is attributable to the formation of metallic fcc (metallic face center cubic) structured Ag metal nanoparticles.[53] On the other hand, the corresponding signals at 31.6, 34.4, 36.4, 47.5, 56.5, 62.8, 67.9, and 76.9° are recognizable for lattice planes of 100, 002, 101, 102, 110, 103, 112, and 202 (JCPDS card no. 36-1451), representing wurtzite ZnO nanoparticles.[54] The obtained values of lattice constants for Ag and ZnO matched well with standard values of pure Ag (PDF# 00-004-0783) and ZnO (PDF# 00-036-1451), respectively. Comparatively, the diffraction pattern of the ANCC/Ag–ZnO nanocomposite (Fig. 5b) shows only minor diffractions at 34.5° (022) and 56.9° (110) for wurtzite ZnO nanoparticles, and the other diffraction signals of ZnO are hardly observed. On the other hand, the diffraction signals due to the metallic Ag

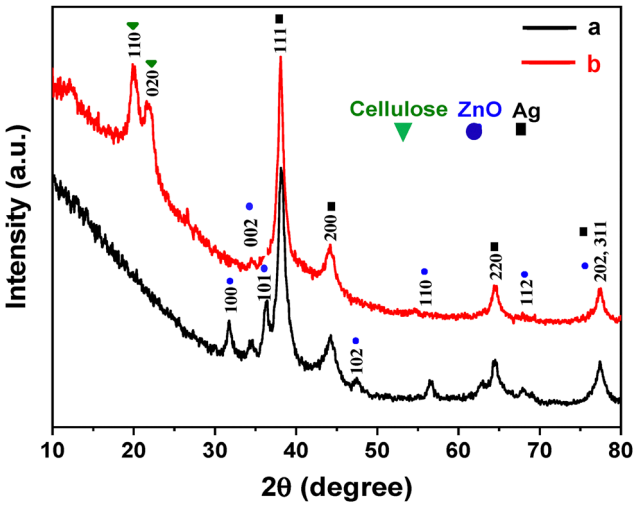

Fig. 5 X-ray diffraction (XRD) patterns of powder deposits obtained from the hybrid Ag–ZnO (a) and ANCC/Ag–ZnO nanocomposite (b) particles at a continuous scan rate of 10° min^{-1}. Conditions: Cu Kα radiation (λ ≫), 1.5406 Å; tube voltage, 33 kV; tube current, 45 mA.

phase in the ANCC/Ag–ZnO nanocomposite remains identical to hybrid Ag–ZnO nanoparticles. The domination of the Ag phase over the ZnO phase originates from the higher atomic size (Zn, 139 pm; Ag, 172 pm) and reduction potential (Zn, −0.76 V; Ag, 0.80 V) of Ag. The average crystallite sizes of Ag and ZnO nanoparticles in the hybrid Ag–ZnO, determined by using the Debye–Scherrer formula, are 6.27 and 10.19 nm, whereas those in the nanocomposite are 9.69 and 3.58 nm, respectively. Coherently the average crystallite sizes of the hybrid Ag–ZnO in reference Ag–ZnO nanoparticles and the ANCC/Ag–ZnO nanocomposite are 8.91 and 7.02 nm, respectively. This reduction in the average crystallite size of the ANCC/Ag–ZnO nanocomposite indicates the improvement in the stability of metal–metal oxide hybrid nanoparticles. The coordination of Ag–ZnO nanoparticles obviously reduces the hydrogen bonding and structural regularity in the cellulose network, and hence, the crystallinity indexes are 73% for ANCC and 69% for the ANCC/Ag–ZnO nanocomposite. The diffraction pattern of the ANCC/Ag–ZnO nanocomposite also shows the characteristic doublets at 20.2 and 22.3°, attributed to (110) and (020) lattice planes of the cellulose Iβ structure.

Electrochemical measurements

The electron transfer between electrolyte and respective graphite coated ANCC, the hybrid Ag–ZnO and the ANC/Ag–ZnO

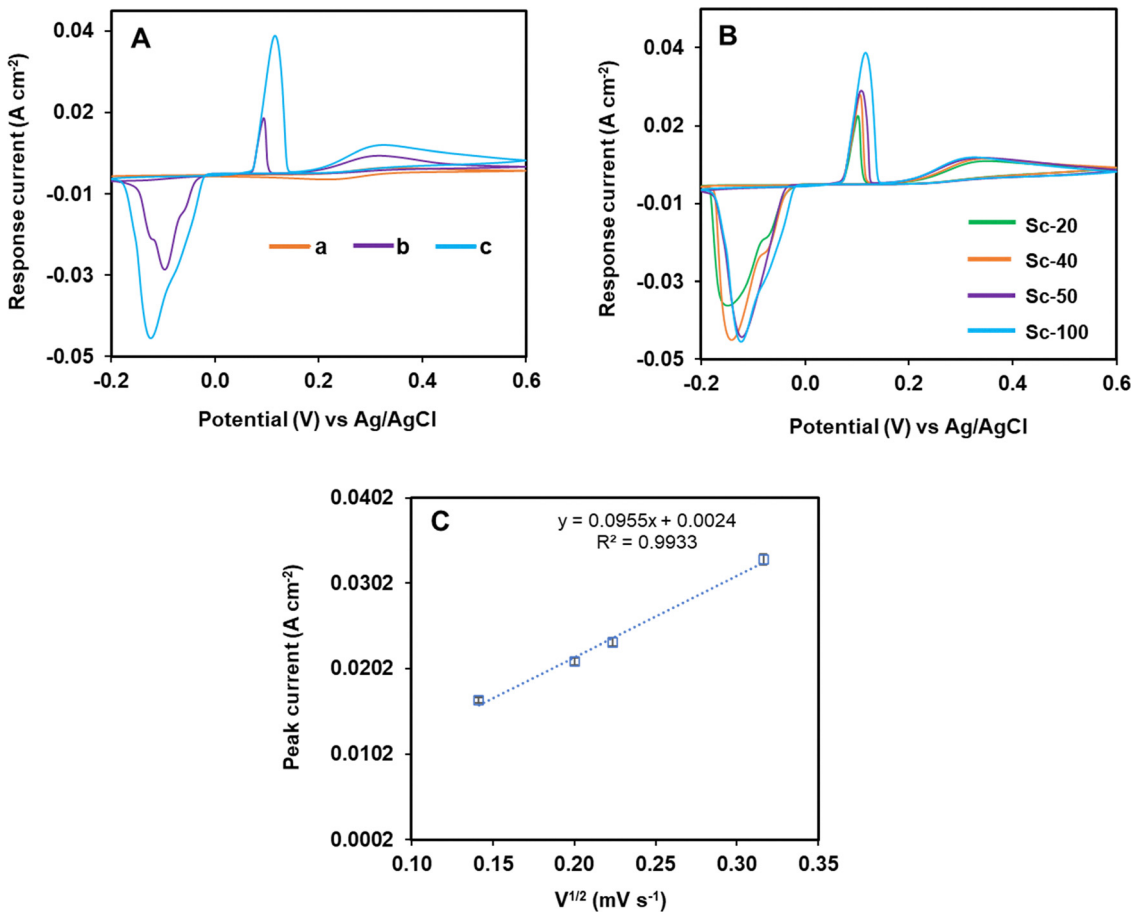

Fig. 6 (A) CV curves of the respective graphite coated ANCC (a), hybrid Ag–ZnO (b) and ANCC/Ag–ZnO nanocomposite (c) electrode in phosphate buffered (pH 7.0) 5.0 mM $[Fe(CN)_6]^{3/4-}$ solution at a scan rate of 100 mV s^{-1}. (B) Scan rate effect on CV curves of the graphite coated ANCC/Ag–ZnO nanocomposite electrode in phosphate buffered (pH 7.0) 5.0 mM $[Fe(CN)_6]^{3/4-}$ solution. (C) A plot of peak current *versus* the square root of the scan rate.

nanocomposite electrode was assessed by monitoring CV curves in phosphate buffered (pH 7.0) 5.0 mM $[Fe(CN)_6]^{3/4-}$ solution and the results are displayed in Fig. 6A. The potential range (−0.2 to +0.6 V) and measurement temperature (25 °C) were kept identical. The sharp anodic and cathodic peaks (I_{pa} and I_{pc}) of $[Fe(CN)_6]^{3/4-}$ at the fabricated working electrodes demonstrate good electron transfer behavior during oxidation–reduction reactions. Among the designed working electrodes, the ANCC exhibits the lowest peak currents (I_{pa}, 1.41 × 10^{-3} A cm^{-2} and I_{pc}, 1.36 × 10^{-3} A cm^{-2}), and hence it is a challenging task to distinguish the redox peaks. Comparatively, the ANCC/Ag–ZnO coated graphite electrode reveals the maximum peak current (I_{pa}, 3.29 × 10^{-2} A cm^{-2} and I_{pc}, 3.98 × 10^{-2} A cm^{-2}), a well distinguishable redox peak. This result indicates that the ANCC/Ag–ZnO nanocomposite facilitates better electron transport behavior from the redox probe $[Fe(CN)_6]^{3/4-}$ solution enroute to the electrode surface following inclusion and stabilization of hybrid Ag–ZnO nanoparticles by functional ANCC, along with the synergetic effect of binary Ag–ZnO and ANCC. The positive role of non-conducting ANCC in enhancing the electrochemical performance is also accompanied by a superior surface-to-volume ratio and porous cellulose structure that favors the transport of electrolyte ions to the inner part of the electrode.[4,55] The above electrochemical results suggest that the graphite coated ANCC/Ag–ZnO nanocomposite electrode is favorably active as a catalytic electrode for electrochemical redox reactions. The enhanced electrochemical performance at the ANCC/Ag–ZnO nanocomposite electrode can also be explained from the comparative study of electroactive surface area (EASA), which was estimated from the respective oxidation peak current (I_{pa}) by using the Randles–Sevcik equation (eqn (1)).[56]

$$I_{pa} = 2.69 \times 10^5 n^{3/2} A D^{1/2} C v^{1/2} \quad (1)$$

Here n is the number of electrons taking part in the redox reaction, A is the EASA (cm^2), D is the diffusion coefficient (6.50 × 10^{-6} cm^2 s^{-1}), C is the redox probe $[Fe(CN)_6]^{3/4-}$ concentration (5 × 10^{-6} mol cm^{-3}) and v is the scan rate (0.1 V s^{-1}). The calculation revealed that the EASA value of the ANCC/Ag–ZnO nanocomposite (9.13 cm^2) is significantly higher than those of both ANCC (1.21 cm^2) and hybrid Ag–ZnO (3.41 cm^2). The higher EASA of the ANCC/Ag–ZnO nanocomposite thus also contributes to higher peak current intensity. The better electron transfer executed by the graphite coated ANCC/Ag–ZnO nanocomposite electrode was further evaluated at various scan rates between 20 and 100 mV s^{-1} in order to comprehend the rate capability, electrocatalytic behavior, sensitivity, and the maximum EASA. Fig. 6B demonstrates that the peak current response increases with the increase in the scan rate, while the shape of the CV curves remains nearly unaltered. The ANCC/Ag–ZnO nanocomposite electrode exhibits both enhanced performance and fair reversibility at higher scan rates up to 100 mV s^{-1}, suggesting that the synthesized nanocomposite possesses favorable electrochemical properties for sensor applications. To further analyze the mechanism, a plot of peak current (I_p) against the square root of scan rate ($v^{1/2}$) was constructed, as shown in Fig. 6C. The peak current (I_p) increases linearly with the scan rate. This suggests that the reaction indicates a diffusion-controlled electrochemical process.

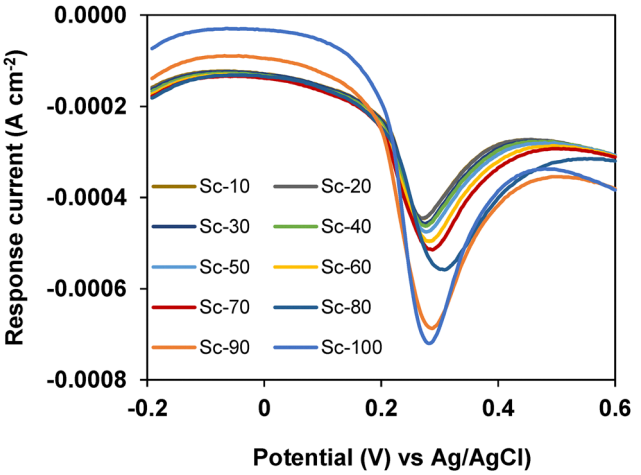

Fig. 7 SWV curves of the graphite coated ANCC/Ag–ZnO nanocomposite electrode in phosphate buffered (pH 7.0) 4.0 mM AA solution at various scan rates.

Fig. 7 shows a series of SWV responses at different scan rates ranging from 10 to 100 mV s^{-1} in the potential range of −0.2 to +0.6 V (*vs.* Ag/AgCl). These curves have been constructed to obtain an idea on reaction kinetics. As can be seen, the oxidation peak current increases progressively with the increase of the scan rate. This behavior indicates that the scan rate influenced the electrode reaction. This also suggests that electron transfer kinetics is favorable at higher scan rates due to reduced diffusion time and that more analyte is oxidized at higher scan rates due to reduced diffusion time.

The conductance of the electrode is a crucial parameter for examining the oxidation/reduction capability of an analyte. As such, the electrochemical impedance spectra (EIS) of the respective graphite coated ANCC, Ag–ZnO and ANCC/Ag–ZnO nanocomposite electrodes were measured in phosphate buffered (pH 7.0) 5.0 mM $[Fe(CN)_6]^{3/4-}$ solution and the obtained results are compared in Fig. 8. The semi-circle diameter of the Nyquist plot in the higher frequency region is due to the charge transfer resistance (R_{ct}) and the slope of the vertical curve at the lower frequency region corresponds to the Warburg resistance (Z_w), which corresponds to the diffusion of electrolyte ions in the electrode material, which always relates to ideal sensor behavior.[57,58] The measured R_{ct} values are 0.12 Ω, 1.31 Ω, and 1.29 Ω for ANCC, Ag–ZnO and ANCC/Ag–ZnO coated electrodes respectively. The comparatively lower R_{ct} value of the ANCC coated electrode is believed to be associated with high crystallinity, large specific surface area and porosity, which promoted rapid electron mobility and efficient charge transfer.[59] The incorporation of ANCC into Ag–ZnO leads to the formation of a nanocomposite structure that leverages the conductive and structural advantages of ANCC along with the catalytic activity of Ag–ZnO. This synergistic interaction leads to a reduced charge transfer resistance in the ANCC/Ag–ZnO electrode,

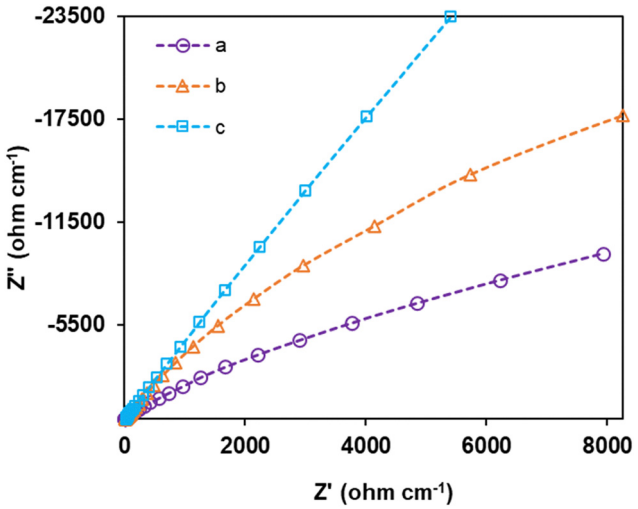

Fig. 8 The Nyquist plots of the EIS of graphite coated ANCC (a), Ag–ZnO (b) and ANCC/Ag–ZnO nanocomposite (c) electrodes in phosphate buffered (pH 7.0) 5.0 mM $[Fe(CN)_6]^{3/4-}$ solution over the frequency range of 5×10^{-2} to 5×10^{-5} Hz measured at a 100 mV s^{-1} scan rate.

indicating improved interfacial charge transport and electrochemical kinetics, an important criterion for high-performance sensor applications. Above all, irrespective of electrode compositions, the value of R_{ct} is very low and almost negligible. The electron-transfer rate constant (k_{ET}), implying the probability of an electron being transferred under given conditions, was calculated using the respective R_{ct} value. The k_{ET} values of ANCC, Ag–ZnO, and ANCC/Ag–ZnO are 2.840, 0.264, and 0.260 s^{-1}, respectively. The higher k_{ET} value of ANCC indicates highly efficient charge transport at the ANCC/electrolyte interface. In contrast, Ag–ZnO showed a lower k_{ET} (0.264 s^{-1}), reflecting sluggish electron-transfer kinetics. The slightly lower k_{ET} value (0.260 s^{-1}) of the ANCC/Ag–ZnO nanocomposite signifies that both Ag–ZnO nanoparticles and ANCC contributed to the electrochemical response. Each electrode exhibits a slightly different gradient in the vertical curve within the low-frequency range. From the resultant EIS in Fig. 8, it is evident that ANCC has a relatively lower slope compared to others and the Nyquist plot of ANCC/Ag–ZnO is closer to the *Y* axis, which provides proof for a relatively higher diffusion rate of electrolyte ions in the electrode material. Hence comparatively, the fabricated electrode using the ANCC/Ag–ZnO nanocomposite has a better electrical conductivity and thus it is relatively suitable for applications in electrochemical sensing.

Based on the above results, the electrochemical measurement of AA with a graphite coated ANCC/Ag–ZnO nanocomposite

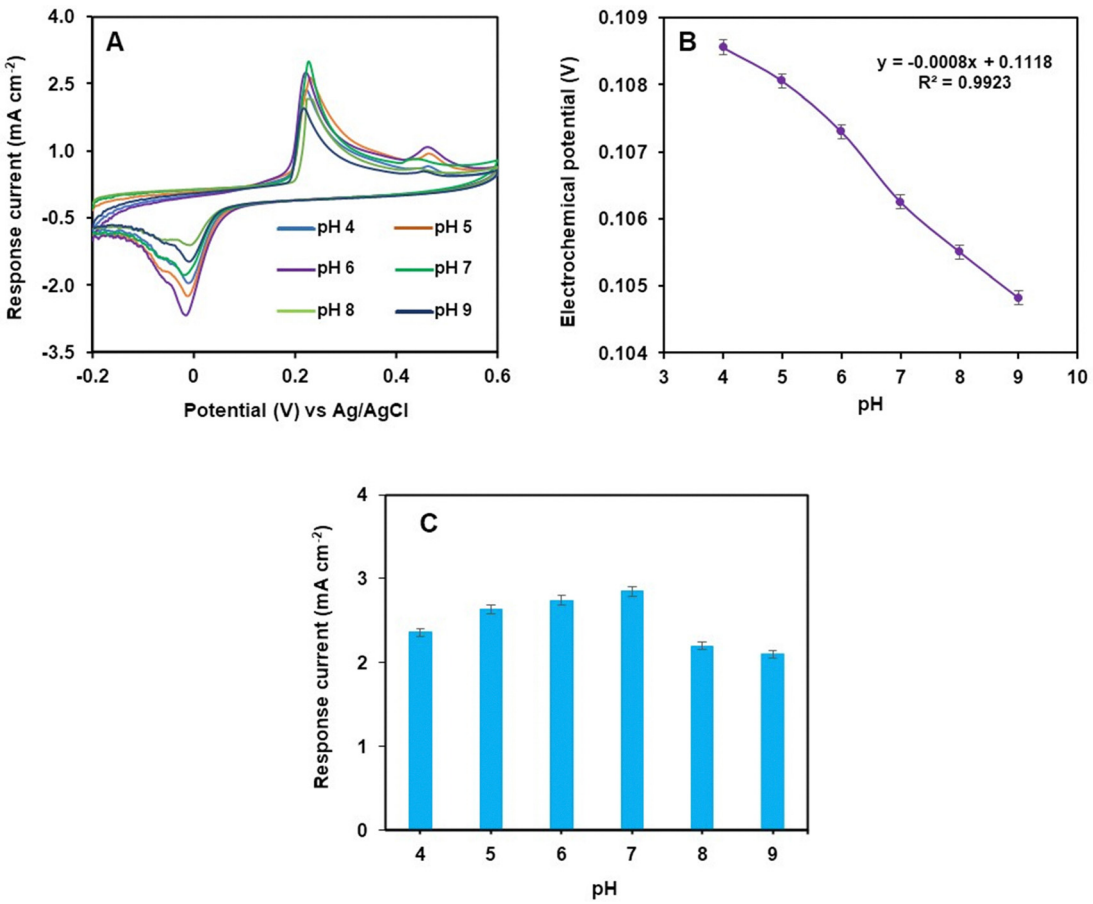

Fig. 9 (A) CV curves of the graphite coated ANCC/Ag–ZnO nanocomposite electrode in phosphate buffered 5.0 mM $[Fe(CN)_6]^{3/4-}$ solution (pH variable) containing 4.0 mM AA at a scan rate of 100 mV s^{-1}. (B) Electrochemical potential, $E_{1/2}$ *versus* pH curve and (C) pH tuning in a bar diagram.

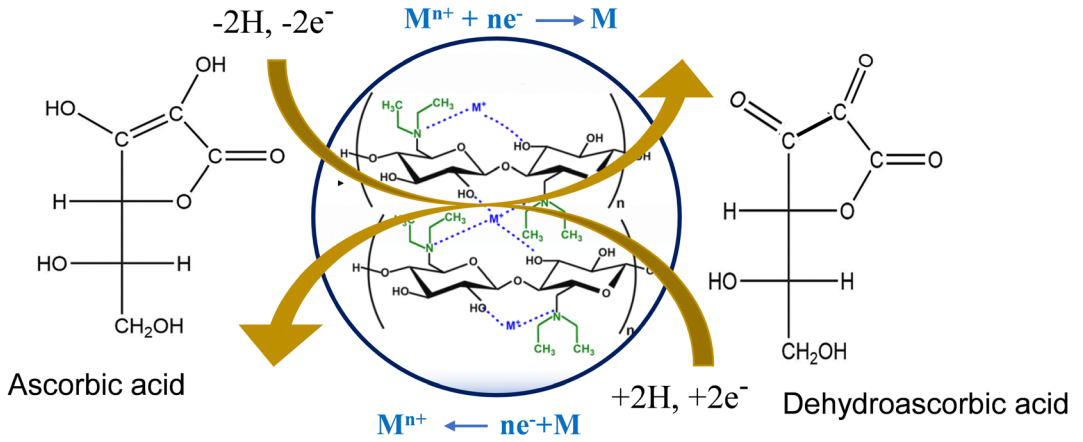

Scheme 1 The possible electrochemical redox mechanism of AA.

electrode is attempted. First, the pH of the buffer solution was optimized to get the highest sensitivity. The pH dependent study was carried out in a phosphate buffer solution of 5.0 mM $[Fe(CN)_6]^{3/4-}$ over the pH range of 4.0–9.0 by adding 4.0 mM AA and the measurement temperature was around 25 °C. The CV curves shown in Fig. 9 indicates that the peak current values improve up to pH 7.0 and then move downward with further increase in pH beyond 7.0. The strong pH dependent peak current demonstrates the involvement of proton transfer during the redox process of the electrochemical reaction.[4,56] It is worth adding that oxidation of AA to dehydro-AA involves the release of 2 electrons and 2 hydrogen ions (Scheme 1). The deprotonation of AA during electrooxidation reduces the electrode reaction in the acidic pH region and hence, ultimately the response current. The finding indicates that phosphate buffer at pH 7.0 is the best choice to obtain the maximum current response and sensitivity. In this context, we can say that the fabricated graphite coated ANCC/Ag–ZnO nanocomposite electrode can be used as a sensor under the physiological pH conditions and pH 7.0 is chosen as the optimum value for the following experiments. Fig. 9B demonstrates the validation of the Nernst equation across the pH range of 4.0–9.0 by measuring the electrochemical potential ($E_{1/2}$). A high regression coefficient of 0.9923 demonstrates an excellent fit of experimental data to the linear relationship as predicted by the Nernst equation. Thus, it strongly supports the validity of the Nernst equation for this particular system and experimental conditions.

The graphite-coated ANCC and ANCC/Ag–ZnO electrodes were submerged separately in a definite volume of phosphate-buffered 5.0 mM $[Fe(CN)_6]^{3/4-}$ (pH 7.0) solution to detect analyte AA for the evaluation of current response capacity. As illustrated in Fig. 10, it is seen that the peak current intensity increases with the increase in AA concentration. Comparatively, the current response achieves the maximum value at the graphite-coated ANCC/Ag–ZnO nanocomposite electrode (21.3 mA cm^{-2}), almost eight times higher than that at the graphite-coated ANCC electrode (2.8 mA cm^{-2}). Hence, the incorporation of binary Ag–ZnO in ANCC dramatically enhances the charge transport between the electrolyte and electrode. Different active polar

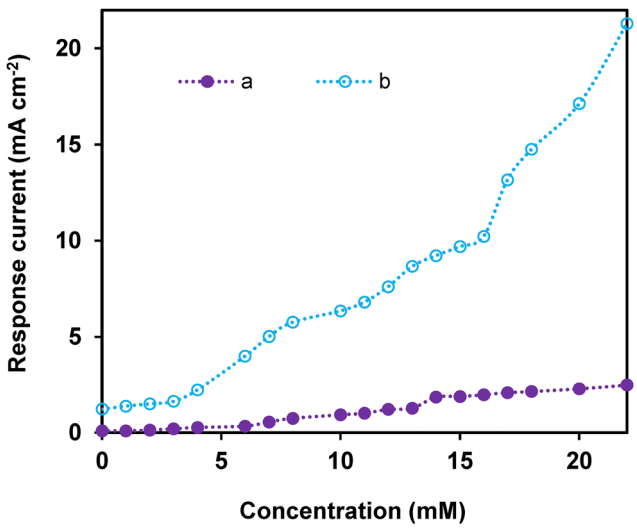

Fig. 10 The variation of response current for graphite coated ANCC (a) and ANCC/Ag–ZnO nanocomposite (b) electrodes with the change in AA concentration in phosphate buffered 5.0 mM $[Fe(CN)_6]^{3/4-}$ solution. Conditions: scan rate, 100 mV s^{-1}; potential, −0.2 to +0.6 V, pH 7.0.

functional groups and porous structures induce greater adsorption or accumulation of analyte AA molecules onto the surface of the ANCC/Ag–ZnO nanocomposite sensor by interacting with the surface functionalities through non-bonding interactions such as hydrogen bonding and polar–polar interactions.[60] The possible electrochemical redox mechanism of AA at the designed electrode is given in Scheme 1. The release of two electrons and two hydrogen ions increases the oxidation current response.[61]

The analytical performance of the graphite coated ANCC/Ag–ZnO nanocomposite was checked by constructing a calibration curve showing the relationship between peak current and AA concentration maintained within the range 0–16.0 mM. The results shown in Fig. 11 represent a linear relation between peak current and the AA concentration with a regression (R^2) value of 0.9934 and a sensitivity factor of 0.543 mA mM^{-1} cm^{-2}. Therefore, it can be said that the graphite coated ANCC/Ag–ZnO nanocomposite electrode worked fairly well in AA detection and

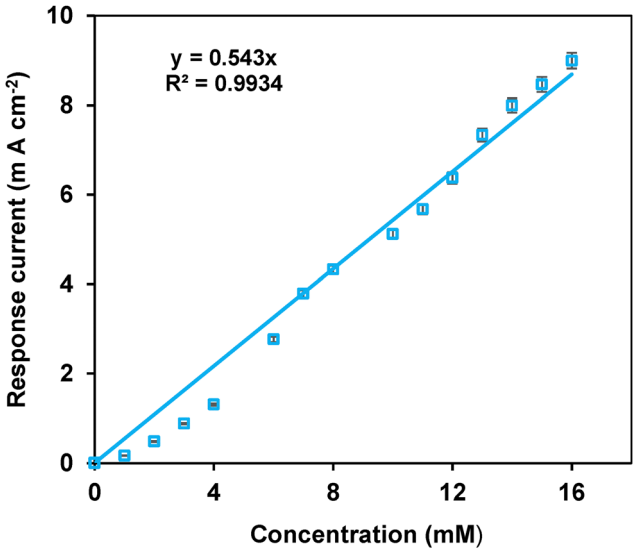

Fig. 11 Calibration curve of response current against variable AA concentration for the graphite coated ANCC/Ag–ZnO nanocomposite electrode in phosphate-buffered 5.0 mM $[Fe(CN)_6]^{3/4-}$ solution. Conditions: scan rate, 100 mV s^{-1}; potential, −0.2 to +0.6 V, pH 7.0.

can be recommended as a reliable and authentic sensor for electrochemical analysis. The limit of detection (LOD), an essential parameter for a sensor, was estimated from eqn (2).

$$\mathrm{LOD} = (K \times S)/m \quad (2)$$

Here, the signal-to-noise ratio (K) is selected as 3 (a confidence level of 98.3%), the standard deviation (S) of the blank *i.e.*, without the substrate is 0.00577 mM from the calibration curve, and the slope (m) of the linear part is 0.543. Hence, mathematically the LOD is calculated to be 0.031 mM.

To achieve good sensing performance by an electrode, one needs to develop an electrode with high sensitivity, minimum LOD, and a wide linear calibration region. Table 1 shows a comparison of the performance of our graphite-coated ANCC/Ag–ZnO nanocomposite electrode with some previously designed electrodes available in the literature. It is observed that our fabricated graphite electrode possessed a sufficiently broad linear range (0–16.0 mM) of AA concentration, a good sign for quantifying the analyte over a wider range. The sensitivity, an important indicator of efficient qualitative and quantitative detection of the analyte, is also reasonably good. The corresponding data on the sensitivity of other prepared electrodes are not adequately addressed. However, it is worth mentioning that our graphite coated nanocomposite electrode possessed better sensitivity than the glassy carbon (GC) modified GO–Ag–Fe_3O_4 electrode. The LOD value of our nanocomposite electrode is slightly high, but still pretty good for application as an electrochemical sensor electrode.

Fig. 12A presents the SWV response of the graphite coated ANCC/Ag–ZnO electrode towards increasing concentrations of AA. As shown in the voltammograms, the peak current increases systematically with rising AA concentration, indicating a well-defined concentration-dependent electrochemical oxidation process. The voltammetric peak appears at a consistent potential (~0.2 V *vs.* reference electrode), suggesting a stable redox behavior of AA at the electrode surface. The increasing intensity of the peak confirms the sensitivity of the sensor towards AA. The corresponding linear relationship between peak current and AA concentration over the tested range shows a high correlation coefficient (R^2) of 0.9924 (Fig. 12B). This confirms that the sensor exhibits a high degree of sensitivity and is well-suited for the quantitative determination of AA.

Reproducibility, selectivity, and stability are all important parameters for an electrode material to be successful as an electrochemical sensor. Reproducibility is the capability to produce an analogous electrochemical signal for consecutive days during analyte (AA) detection. The CV curves illustrated in Fig. 13A show a relative standard deviation (RSD) value of the peak current of 2.06%, which is below the 5% acceptable level. This result proves the trustworthiness and reliability of the designed graphite-coated ANCC/Ag–ZnO nanocomposite electrode as a sensor material.

The accuracy of all conditions, such as applied voltage and buffer environment, is very important for the determination of a definite analyte in real applications. Thus, the selectivity of the graphite coated ANCC/Ag–ZnO nanocomposite electrode sensor for the selective detection of AA in a complex mixture is to be justified. For this, the anti-interfering capacity of the fabricated nanocomposite electrode was evaluated in the

Table 1 Comparison of electrode performance with some reported literature values

Electrode	Sensitivity (mA mM^{-1} cm^{-2})	LOD (mM)	Linear range (mM)	Ref.
ZnO NPs/GCE	—	0.0184	0.05–1.0	62
Cu–Ag/rGO	—	0.0036	0.005–0.03	63
CoPtNPs/Pt	0.103	0.00037	0.01–0.5	64
Ag_2S–CuO–ZnO/GCE	—	0.00073	0.001–0.15	11
GO–Ag–Fe_3O_4/GCE	1.1468	0.000074	0.0002–0.06	65
Fe-doped CuO/GCE	—	0.00466	0.005–0.05	66
ERGO/Fe–Fe_2O_3/GCE	—	0.00593	0.05–10.0	67
Au–Cu_2O/MWCNTs/GCE	—	0.0003	0.0001–0.2	68
Co–N/Zn@NPC/GCE	—	0.0000076	0.0001–0.1571	69
Graphite-coated ANCC/Ag–ZnO	0.543	0.031	0–16.0	This work

Note: GCE = glassy carbon electrode, rGO = reduced graphene oxide, MWCNTs = multi-walled carbon nanotubes, NPC = nanoporous carbon.

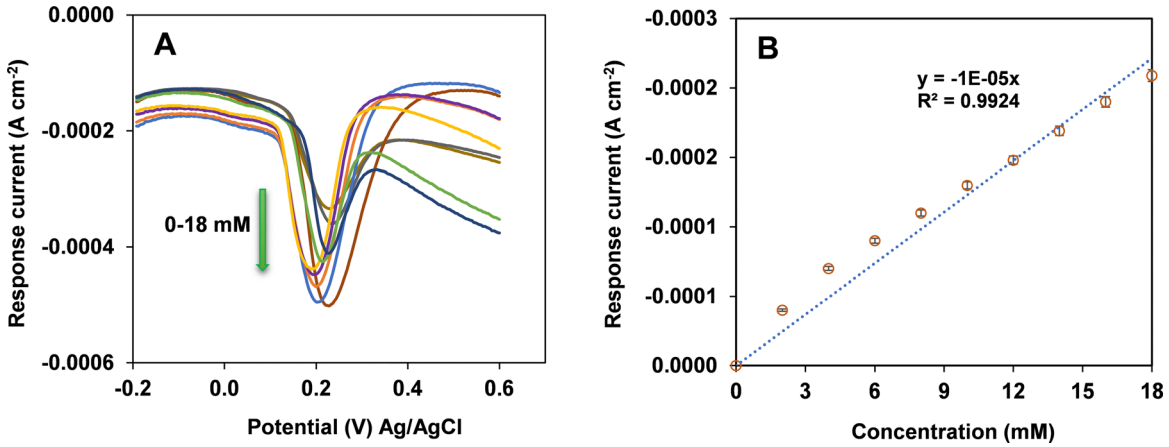

Fig. 12 (A) SWV responses of the graphite coated ANCC/Ag–ZnO nanocomposite electrode towards increasing concentrations of AA in 0.1 M phosphate buffer at pH 7.0. The arrow indicates the direction of increasing AA concentration. (B) The corresponding calibration curve shows a linear relationship between peak current and AA concentration. Conditions: scan rate 100 mV s^{-1}.

presence of some possible interfering compounds like sucrose, D-glucose, and uric acid (UA). The concentrations of interfering compounds and that of AA were kept identical at 1.0 mM and the measurement was carried out in phosphate buffered solution at pH 7.0 with the scan rate being fixed at 100 mV s^{-1}. Fig. 13B reveals that the CV current response of interfering compounds is insignificant in comparison to AA. Therefore, the graphite coated ANCC/Ag–ZnO nanocomposite

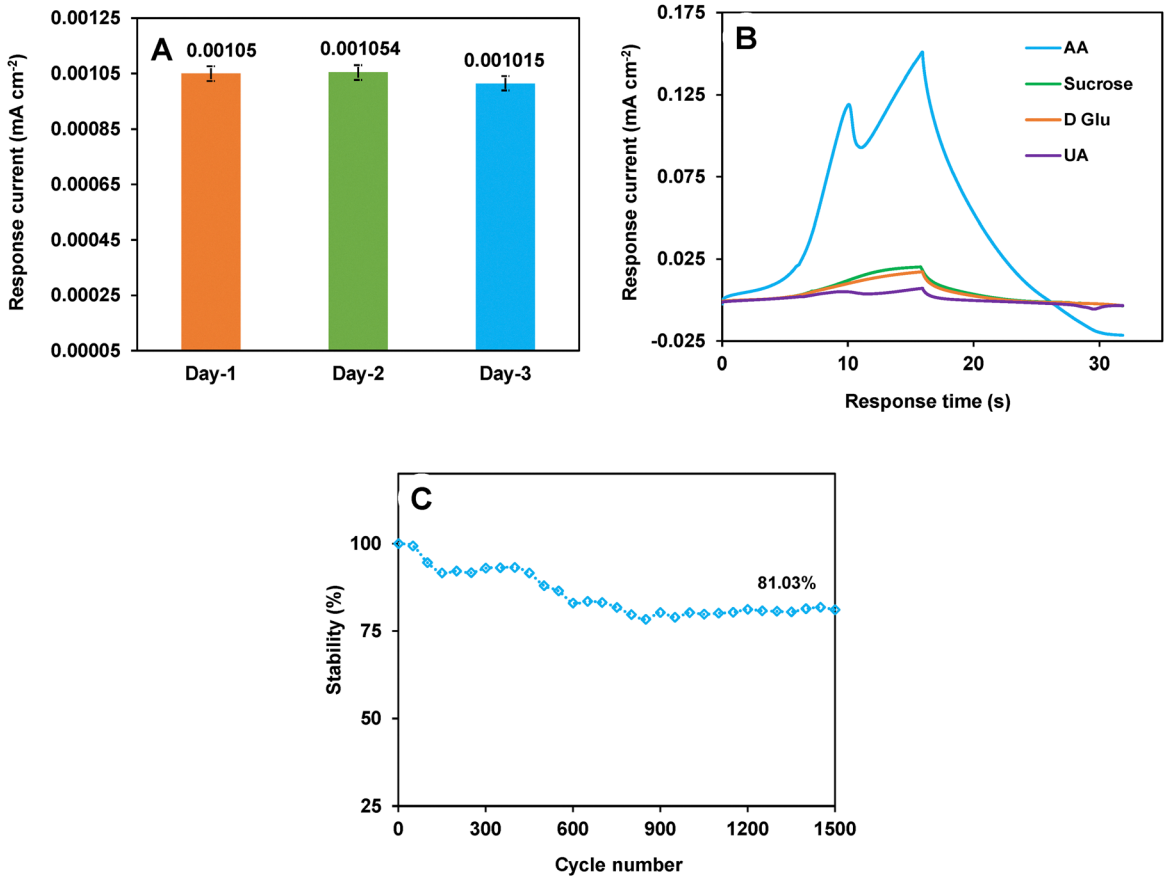

Fig. 13 (A) Reproducibility of CV curves of the graphite coated ANCC/Ag–ZnO nanocomposite electrode dipped in phosphate-buffered 5.0 mM $[Fe(CN)_6]^{3/4-}$ solution containing 4.0 mM AA. (B) Change in the oxidation current response in the presence of 1.0 mM of the respective AA and interfering substance in the potential range of −0.2 to +0.6 V. (C) Retention of response current over an extended number of cycles at the potential of −0.2 to +0.6 V. Conditions: scan rate, 100 mV s^{-1}; pH 7.0.

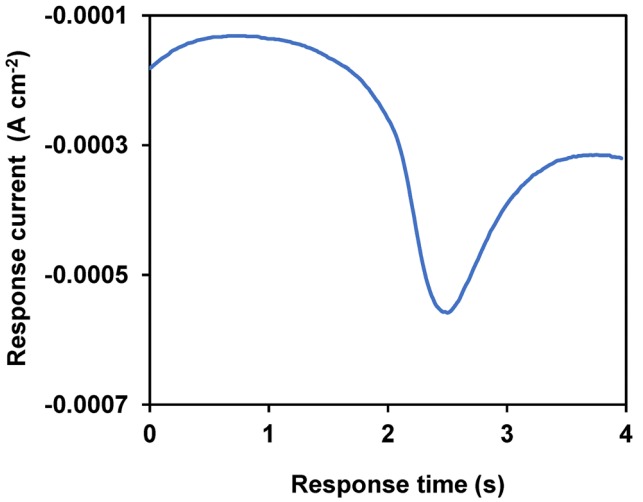

Fig. 14 Response time profile of the graphite coated ANCC/Ag–ZnO nanocomposite electrode upon exposure to phosphate buffered solution (pH 7.0) containing 4.0 mM AA. Conditions: scan rate 100 mV s^{-1}.

electrode sensor suffers almost no interference from these fast electron transfer species during the detection of AA. This result demonstrates the good anti-interfering capacity of the prepared nanocomposite.

The stability of the ANCC/Ag–ZnO nanocomposite electrode sensor is another required criterion, and it was tested *via* a continuous CV method in phosphate-buffered 5.0 mM $[Fe(CN)_6]^{3/4-}$ solution (pH 7.0) containing 4.0 mM AA. The peak current response was monitored, and the peak current retention as a measure of stability is given in Fig. 13C. About 81% of the initial current response value is retained after 1500 cycles of detection. The color of the electrolyte media did not change following repeated cycling measurements, indicating that peeling off of the electrode material did not occur. In another stability test, the freshly prepared graphite coated ANCC/Ag–ZnO nanocomposite electrode was housed in a refrigerator for four weeks at 4 °C. The extended period of stability of the ANCC/Ag–ZnO nanocomposite electrode sensor exhibited an identical response to the initial response. The comprehensive stability of ANCC/Ag–ZnO as a sensor electrode material is thus good enough for electrochemical detection of a biological analyte.

The response time, t_R, of the graphite coated ANCC/Ag–ZnO electrode towards AA was evaluated using a single SWV scan after analyte injection, as presented in Fig. 14. Following the introduction of AA, the sensor exhibited a rapid increase in current, reached its peak value within 3 seconds, indicating a rapid and sensitive electrochemical response suitable for real-time or flow-based sensing applications.

For the real sample analysis, the fabricated ANCC/Ag–ZnO nanocomposite coated battery electrode sensor was used to analyze blood serum containing various known concentrations of AA. The blood samples were prepared in phosphate buffered solution at pH 7.0. The resulting values are evaluated in percentage terms against the known values. A blank electrochemical analysis was performed before real blood sample analysis. The measurement values are presented in Table 2. It is evident that the electrochemical method gives value close to the real concentration value. Hence, the ANCC/Ag–ZnO nanocomposite can be useful in designing sensor probes for clinical applications.

Table 2 Analytical results of AA estimation in reference samples using the ANCC/Ag–ZnO nanocomposite coated battery electrode sensor

Reference sample code	Proposed method conc. (mM)	Real conc. (mM)	RSD (%)
1	0.59	0.5	4.47
2	1.99	2.0	0.37
3	2.45	2.5	2.35
4	4.06	4.0	2.76
5	4.99	5.0	0.28
6	4.98	5.0	1.20
7	5.97	6.0	1.47

Note: RSD = relative standard deviation.

Conclusion

Here, an aminated nanocrystalline cellulose stabilized binary Ag–ZnO nanocomposite, named ANCC/Ag–ZnO, has been used for coating the graphite electrode and applied to quantify AA *via* electrochemical sensing. The NCC, prepared from raw rice (*Oryza sativa*) straw through successive alkali treatment, bleaching, and H_2SO_4 (60%) hydrolysis, is amine functionalized to generate ANCC for facilitating the strong binding with binary hybrid Ag–ZnO nanoparticles. The resultant ANCC/Ag–ZnO nanocomposite is finally obtained *via* a green reduction protocol using the ethanol extract of mussaenda flower (*M. erythrophylla*) bracts. The average size of the ANCC/Ag–ZnO nanocomposite is around 9.77 nm, fairly spherical as measured from TEM. The EDX analysis of the nanocomposite confirmed the existence of Ag (2.6 at%) and Zn (0.17 at%) along with carbon and oxygen. The average crystallite size of binary Ag–ZnO in the nanocomposite is 7.02 nm, and the degree of crystallinity of the nanocomposite is 69%, slightly decreased from 73% in ANCC. A comparative CV analysis among graphite-coated ANCC, Ag–ZnO and the ANCC/Ag–ZnO nanocomposite showed enhanced electron transfer capacity from the nanocomposite electrode due to the synergistic effect of binary Ag–ZnO and ANCC. In the electrochemical sensing of AA, the graphite coated nanocomposite electrode (21.3 mA cm^{-2}) demonstrated an around 8-fold increase in current response compared to the native ANCC electrode (2.8 mA cm^{-2}) and showed good electrocatalytic properties in the linear range of 0–16.0 mM. Additionally, the nanocomposite electrode possessed fairly good sensitivity (0.543 mA mM^{-1} cm^{-2}), good LOD (0.031 mM) and good reproducibility with an RSD value of 2.06%. The nanocomposite electrode demonstrated excellent selectivity towards AA in the presence of other interfering electroactive biological molecules. Meanwhile, the response current, observed from SWV measurement, reached its peak value within 3 seconds of AA injection. The graphite modified nanocomposite electrode thus favored a rapid and sensitive

electrochemical process. In summary, we can say that the synthesized ANCC/Ag–ZnO nanocomposite material can be used to fabricate electrode materials for electrochemical sensing and quantification of AA in biological samples.

Author contributions

Md. Mahabur Rahman: methodology, investigation, formal analysis, data curation, validation, writing – original draft; Md. Sohel Rana: methodology, investigation, formal analysis, data curation, validation; Hideto Minami: investigation, formal analysis, data curation; Md. Mahbubor Rahman: resources, supervision; Md. Abdur Rahman: resources, visualization; Md. Ashraful Alam: resources, visualization; Hasan Ahmad: conceptualization, data curation, formal analysis, resources, supervision, writing – review and editing.

Conflicts of interest

The authors declare no competing financial interest.

Data availability

The data used to support the findings of this study are included within the article.

Acknowledgements

The author (HA) acknowledges instrument support from the Central Science Laboratory, Rajshahi University. The author (HA) acknowledges the research grant under special allocation (FY 2024–2025) from UGC, Dhaka.

References

1 A. Hatefi-Mehrjardi, M. A. Karimi, M. Soleymanzadeh and A. Barani, Highly sensitive detection of dopamine, ascorbic and uric acid with a nanostructure of dianix yellow/multi-walled carbon nanotubes modified electrode, *Measurement*, 2020, **163**, 107893, DOI: 10.1016/j.measurement.2020.107893.

2 G. A. El-Fatah, H. S. Magar, R. Y. A. Hassan, R. Mahmoud, A. A. Farghali and M. E. M. Hassouna, A novel gallium oxide nanoparticles-based sensor for the simultaneous electrochemical detection of Pb^{2+}, Cd^{2+} and Hg^{2+} ions in real water samples, *Sci. Rep.*, 2022, **12**, 20181, DOI: 10.1038/s41598-022-24558-y.

3 S. M. Siddeeg, N. S. Alsaiari, M. A. Tahoon and F. B. Rebah, The application of nanomaterials as electrode modifiers for the electrochemical detection of ascorbic acid: Review, *Int. J. Electrochem. Sci.*, 2020, **15**(4), 3327–3346, DOI: 10.20964/2020.04.13.

4 S. Ponnada, S. Rajagopal, D. B. Gorle, M. S. Kiai, R. K. Sharma and A. Nowduri, A facile, cost-effective, rapid, single-step synthesis of Ag–Cu decorated ZnO nanoflower-like composites (NFLCs) for electrochemical sensing of dopamine, *Mater. Adv.*, 2021, **2**(18), 5986–5996, DOI: 10.1039/D1MA00319D.

5 H. S. Magar, M. E. Ghica, M. N. Abbas and C. M. A. Brett, Highly sensitive choline oxidase enzyme inhibition biosensor for lead ions based on multiwalled carbon nanotube modified glassy carbon electrodes, *Electroanalysis*, 2017, **29**(7), 1741–1748, DOI: 10.1002/elan.201700111.

6 H. S. Magar, M. N. Abbas, M. B. Ali and M. A. Ahmed, Picomolar-sensitive impedimetric sensor for salivary calcium analysis at POC based on SAM of Schiff base-modified gold electrode, *J. Solid State Electrochem.*, 2020, **24**(3), 723–737, DOI: 10.1007/s10008-020-04500-w.

7 A. M. Fahim, H. S. Magar and N. H. Mahmoud, Synthesis, antimicrobial, antitumor activity, docking simulation, theoretical studies, and electrochemical analysis of novel Cd(II), Co(II), Cu(II), and Fe(III) complexes containing barbituric moiety, *Appl. Organomet. Chem.*, 2023, **37**(4), e7023, DOI: 10.1002/aoc.7023.

8 H. S. Magar, E. E. Abu-El Magd, R. Y. A. Hassaan and A. M. Fahim, Rapid impedimetric detection of cadmium ions using nanocellulose/ligand/nanocomposite (CNT/Co_3O_4), *Microchem. J.*, 2022, **182**, 107885, DOI: 10.1016/j.microc.2022.107885.

9 H. S. Magar, H. Abdelghany, M. N. Abbas, U. Bilitewski and R. Y. A. Hassan, Fast analysis of Staphylococcus aureus in food products using disposable label-free nano-electrochemical immunosensor chips, *Microchem. J.*, 2023, **193**, 109097, DOI: 10.1016/j.microc.2023.109097.

10 T. A. Silva, M. R. K. Khan, O. Fatibello-Filhoa and M. M. Collinson, Simultaneous electrochemical sensing of ascorbic acid and uric acid under biofouling conditions using nanoporous gold electrodes, *J. Electroanal. Chem.*, 2019, **846**, 113160, DOI: 10.1016/j.jelechem.2019.05.042.

11 A. Abamecha, A. A. Yimer, G. G. Muleta and S. A. Kitte, Electrochemical determination of ascorbic acid at Ag_2S-CuO-ZnO ternary nanocomposite modified glassy carbon electrode, *Sci. Afr.*, 2025, **28**, e02669, DOI: 10.1016/j.sciaf.2025.e02669.

12 F. Meng, W. Shi, Y. Sun, X. Zhu, G. Wu, C. Ruan, X. Liu and D. Ge, Nonenzymatic biosensor based on Cu_xO nanoparticles deposited on polypyrrole nanowires for improving detectionrange, *Biosens. Bioelectron.*, 2013, **42**, 141–147, DOI: 10.1016/j.bios.2012.10.051.

13 K. Ghanbari and N. Hajheidari, ZnO–Cu_xO/polypyrrole nanocomposite modified electrode for simultaneous determination of ascorbic acid, dopamine, and uric acid, *Anal. Biochem.*, 2015, **473**, 53–62.

14 I. Fernández, J. L. González-Mora, P. Lorenzo-Luis, R. Villalonga and P. A. Salazar-Carballo, Nickel oxide nanoparticles-modified glassy carbon electrodes for non-enzymatic determination of total sugars in commercial beverages, *Microchem. J.*, 2020, **159**, 105538, DOI: 10.1016/j.microc.2020.105538.

15 C.-L. Sun, H.-H. Lee, J.-M. Yang and C.-C. Wu, The simultaneous electrochemical detection of ascorbic acid, dopamine, and uric acid using graphene/size-selected Pt nanocomposites, *Biosens. Bioelectron.*, 2011, **26**, 3450–3455, DOI: 10.1016/j.bios.2011.01.023.

16 H. Sun, H. Liu, M. Fang, Z. Chen, Y. Zhang and X. Tan, Electrochemical sensor of Cu nanoparticles on Cu based metal organic frame works hybridized indium tin oxides glasses for Pb^{2+} detection, *J. Environ. Chem. Eng.*, 2024, **12**(2), 112069, DOI: 10.1016/j.jece.2024.112069.

17 R. Gupta, P. K. Rastogi, V. Ganesan, D. K. Yadav and P. K. Sonkar, Gold nanoparticles decorated mesoporous silica microspheres: A proficient electrochemical sensing scaffold for hydrazine and nitrobenzene, *Sens. Actuators, B*, 2017, **239**, 970–978, DOI: 10.1016/j.snb.2016.08.117.

18 A. Abbas and H. M. A. Amin, Silver nanoparticles modified electrodes for electroanalysis: An updated review and a perspective, *Microchem. J.*, 2022, **175**, 107166, DOI: 10.1016/j.microc.2021.107166.

19 S. Lee, J. Oh, D. Kim and Y. Piao, A sensitive electrochemical sensor using an iron oxide/graphene composite for the simultaneous detection of heavy metal ions, *Talanta*, 2016, **160**, 528–536, DOI: 10.1016/j.talanta.2016.07.034.

20 L. A. Mohammed, A. H. Majeed, O. G. Hammoodi, C. Prakash, M. A. Alheety, D. Buddhi, S. A. Dhadoosh and I. K. Mohammed, Design and characterization of novel ternary nanocomposite (rGO-MnO_2-PoPDA) product and screening its dielectric properties, *Int. J. Interact. Des. Manuf.*, 2023, **17**, 2387–2401, DOI: 10.1007/s12008-022-01020-x.

21 R. Mohanraj, R. Brindha, R. Kandeeban, M. Mahendhar, K. Saminathan and G. Ayyappadasan, Electrochemical detection of 5-hydroxytryptamine using sustainable SnO_2-Graphite nanocomposite modified electrode, *Mater. Lett.*, 2021, **305**, 130796, DOI: 10.1016/j.matlet.2021.130796.

22 K. G. Manjunatha, B. E. K. Swamy, G. K. Jayaprakash, S. C. Sharma, P. Lalitha and K. A. Vishnumurthy, Electrochemical determination of paracetamol at Cu doped ZnO/Nanoparticle with TX-100-surfactant MCPE: A cyclic voltammetric technique, *Inorg. Chem. Commun.*, 2022, **142**, 109630, DOI: 10.1016/j.inoche.2022.109630.

23 R. Mayilduri, S. Mahalakshmi, T. Maruthavanan, K. K. Vijayakumari, R. Priya, M. Ramesh and C. Sankar, Highly sensitive electrochemical detection of monosodium glutamate and nitrite on a binary metal (FeZnO) nanocomposite, *New J. Chem.*, 2025, **49**(15), 6178–6186, DOI: 10.1039/D5NJ00212E.

24 P. Singh, S. Mandal, D. Roy and N. Chanda, Facile detection of blood creatinine using binary copper–iron oxide and rGO-based nanocomposite on 3D printed Ag-electrode under POC settings, *ACS Biomater. Sci. Eng.*, 2021, **7**(7), 3446–3458, DOI: 10.1021/acsbiomaterials.1c00484.

25 G. Maduraiveeran and A. Chen, Design of an enzyme-mimicking NiO@Au nanocomposite for the sensitive electrochemical detection of lactic acid in human serum and urine, *Electrochim. Acta*, 2021, **368**, 137612, DOI: 10.1016/j.electacta.2020.137612.

26 S. K. Ponnaiah, P. Periakauppan and B. Vellaichamy, New electrochemical sensor based on a silver-doped iron oxide nanocomposite coupled with polyaniline and its sensing application for picomolar-level detection of uric acid in human blood and urine samples, *J. Phys. Chem. B*, 2018, **122**(12), 3037–3046, DOI: 10.1021/acs.jpcb.7b11504.

27 R. Abdel-Hameed, A. M. Ashmawy, M. AlElaimi, N. M. Abourashed, A. Hegazy, O. A. O. Alshammari, A. Tantawy, E. Elgazzar, H. A. Batakoushy, A. E. F. Abbas and A. M. Abdel-Raoof, Electrochemical platform with Ag/ZnO nanorods for green, blue, and white determination of the newly approved drug roxadustat in pharmaceuticals and plasma: NQS assessment and UN-SDGs alignment, *Microchem. J.*, 2025, **212**, 113326, DOI: 10.1016/j.microc.2025.113326.

28 K. Vijayalakshmi, S. Radha and K. Muthumeenakshi, Environmentally friendly synthesis of Ag–ZnO nanocomposite-modified graphite electrode for copper ion quantification, *J. Mater. Sci.: Mater. Electron.*, 2025, **36**(12), 697, DOI: 10.1007/s10854-025-14771-6.

29 Y. Ni, J. Xu, H. Liu and S. Shao, Fabrication of RGO-$NiCo_2O_4$ nanorods composite from deep eutectic solvents for nonenzymatic amperometric sensing of glucose, *Talanta*, 2018, **185**, 335–343, DOI: 10.1016/j.talanta.2018.03.097.

30 W. Zhu, Y. Zhou, M. Tao, X. Yan, Y. Liu and X. Zhou, An electrochemical and fluorescence dual-signal assay based on Fe_3O_4@MnO_2 and N-doped carbon dots for determination of hydrogen peroxide, *Microchim. Acta*, 2020, **187**(3), 187, DOI: 10.1007/s00604-020-4163-5.

31 R. Sasikumar, B. Kim and A. Ishfaque, Active-site-rich binary metal oxides integrated organic–inorganic hybrid nanocomposite: Electrochemical simultaneous detection of multi-drugs of isoprenaline and resorcinol in real samples, *Microchem. J.*, 2023, **187**, 108375, DOI: 10.1016/j.microc.2022.108375.

32 M. S. Rana, M. A. Rabbi, M. F. Begum, H. Minami, S. M. Hoque, M. M. Rahman, M. A. Rahman and H. Ahmad, Aminated nano-crystalline cellulose decorated binary Ag-ZnO nanocomposite particles with a comparative study of antimicrobial activity and cell viability, *Carbohydr. Polym. Technol. Appl.*, 2024, **8**, 100554, DOI: 10.1016/j.carpta.2024.100554.

33 I. L. T. Bouzeko, F. L. M. Dongmo, B. L. Ndontsa, C. A. N. Ngansop and R. Keumoe, *et al.*, Chemical constituents of *Mussaenda erythrophylla* Schumach. & Thonn. (Rubiaceae) and their chemophenetic significance, *Biochem. Syst. Ecol.*, 2021, **98**, 104329, DOI: 10.1016/j.bse.2021.104329.

34 S. Kamel and T. A. Khattab, Recent advances in cellulose-based biosensors for medical diagnosis, *Biosensors*, 2020, **10**(6), 67, DOI: 10.3390/bios10060067.

35 M. A. Rabbi, M. M. Rahman, H. Minami, M. A. Rahman, S. M. Hoque and H. Ahmad, Biocomposites of synthetic polymer modified microcrystalline jute cellulose particles and their hemolytic behavior, *Cellulose*, 2019, **26**(16), 8713–8727, DOI: 10.1007/s10570-019-02706-4.

36 B. Joseph, V. K. Sagarika, C. Sabu, N. Kalarikkal and S. Thomas, Cellulose nanocomposites: Fabrication and biomedical applications, *J. Bioresour. Bioprod.*, 2020, **5**(4), 223–237, DOI: 10.1016/j.jobab.2020.10.001.

37 Y. Jiang, X. Xiao, C. Li, Y. Luo, S. Chen, G. Shi, K. Han and H. Gu, Facile ratiometric electrochemical sensor for in vivo/online repetitive measurements of cerebral ascorbic acid in brain microdiaysate, *Anal. Chem.*, 2020, **92**(5), 3981–3989, DOI: **10.1021/acs.analchem.9b05484**.

38 C. J. Rebouche, Ascorbic acid and carnitine biosynthesis, *Am. J. Clin. Nutr.*, 1991, **54**(6), 1147S–1152S, DOI: **10.1093/ajcn/54.6.1147s**.

39 K. Dhara and R. M. Debiprosad, Review on nanomaterials-enabled electrochemical sensors for ascorbic acid detection, *Anal. Biochem.*, 2019, **586**, 113415, DOI: **10.1016/j.ab.2019.113415**.

40 H. S. Magar, A. M. Fahim and M. S. Hashem, Accurate, affordable, and easy electrochemical detection of ascorbic acid in fresh fruit juices and pharmaceutical samples using an electroactive gelatin sulfonamide, *RSC Adv.*, 2024, **14**(54), 39820–39832, DOI: **10.1039/D4RA06271J**.

41 V. Arabali, M. Ebrahimi, M. Abbasghorbani, V. K. Gupta, M. Farsi, M. R. Ganjali and F. Karimi, Electrochemical determination of vitamin C in the presence of NADH using a CdO nanoparticle/ionic liquid modified carbon paste electrode as a sensor, *J. Mol. Liq.*, 2016, **213**, 312–316, DOI: **10.1016/j.molliq.2015.10.001**.

42 M. A. Ross, Determination of ascorbic acid and uric acid in plasma by high-performance liquid chromatography, *J. Chromatogr. B: Biomed. Sci. Appl.*, 1994, **657**(1), 197–200, DOI: **10.1016/0378-4347(94)80087-1**.

43 J. Lykkesfeldt, Determination of ascorbic acid and dehydroascorbic acid in biological samples by high-performance liquid chromatography using subtraction methods: reliable reduction with tris[2-carboxyethyl]phosphine hydrochloride, *Anal. Biochem.*, 2000, **282**(1), 89–93, DOI: **10.1006/abio.2000.4592**.

44 F. Nazir and M. Iqbal, Synthesis, characterization and cytotoxicity studies of aminated microcrystalline cellulose derivatives against melanoma and breast cancer cell lines, *Polymers*, 2020, **12**(11), 2634, DOI: **10.3390/polym12112634**.

45 P. Lu and Y.-L. Hsieh, Preparation and characterization of cellulose nanocrystals from rice straw, *Carbohydr. Polym.*, 2012, **87**(1), 564–573, DOI: **10.1016/j.carbpol.2011.08.022**.

46 M. A. Rabbi, M. M. Rahman, H. Minami, N. Yamashita, M. R. Habib and H. Ahmad, Magnetically responsive antibacterial nanocrystalline jute cellulose nanocomposites with moderate catalytic activity, *Carbohydr. Polym.*, 2021, **251**, 117024, DOI: **10.1016/j.carbpol.2020.117024**.

47 M. A. Rabbi, M. M. Rahman, H. Minami, M. R. Habib and H. Ahmad, Ag impregnated sub-micrometer crystalline jute cellulose particles: Catalytic and antibacterial properties, *Carbohydr. Polym.*, 2020, **233**, 115842, DOI: **10.1016/j.carbpol.2020.115842**.

48 S. Rashid and H. Dutta, Characterization of nanocellulose extracted from short, medium and long grain rice husks, *Ind. Crops Prod.*, 2020, **154**, 112627, DOI: **10.1016/j.indcrop.2020.112627**.

49 F. Lughmani, F. Nazir, S. A. Khan and M. Iqbal, Novel functionalized cellulose derivatives fabricated with Cu nanoparticles: synthesis, characterization and degradation of organic pollutants, *Cellulose*, 2022, **29**(3), 1911–1928, DOI: **10.1007/s10570-021-04388-3**.

50 S. Sarkar, E. Guibal, F. Quignard and A. K. SenGupta, Polymer-supported metals and metal oxide nanoparticles: Synthesis, characterization, and applications, *J. Nanopart. Res.*, 2012, **14**, 715, DOI: **10.1007/s11051-011-0715-2**.

51 O. V. D. Berg, J. R. Capadona and C. Weder, Preparation of homogeneous dispersions of tunicate cellulose whiskers in organic solvents, *Biomacromolecules*, 2007, **8**(4), 1353–1357, DOI: **10.1021/bm061104q**.

52 M. Z. Sarker, M. M. Rahman, H. Minami, T. Suzuki and H. Ahmad, Amine functional silica-supported bimetallic Cu-Ni nanocatalyst and investigation of some typical reductions of aromatic nitro-substituents, *Colloid Polym. Sci.*, 2022, **300**(4), 279–296, DOI: **10.1007/s00396-021-04910-w**.

53 F. Fu, J. Gu, J. Cao, R. Shen, H. Liu, Y. Zhang, X. Liu and J. Zhou, Reduction of silver ions using an alkaline cellulose dope: straightforward access to Ag/ZnO decorated cellulose nanocomposite film with enhanced antibacterial activities, *ACS Sustainable Chem. Eng.*, 2018, **6**(1), 738–748, DOI: **10.1021/acssuschemeng.7b03059**.

54 D. Lin, H. Wu, R. Zhang and W. Pan, Enhanced photocatalysis of electrospun Ag–ZnO heterostructured nanofibers, *Chem. Mater.*, 2009, **21**(15), 3479–3484, DOI: **10.1021/cm900225p**.

55 M. Rashid, M. M. Islam, H. Minami, M. Aftabuzzaman, M. A. Rahman, M. M. Hossain, S. M. Hoque, M. Alam and H. Ahmad, Nickel decorated melamine-formaldehyde resin/polyaniline composites for high specific capacitance, *Mater. Chem. Phys.*, 2020, **249**, 122957, DOI: **10.1016/j.matchemphys.2020.122957**.

56 X. Zhang, Y.-C. Zhang and L.-X. Ma, One-pot facile fabrication of graphene-zinc oxide composite and its enhanced sensitivity for simultaneous electrochemical detection of ascorbic acid, dopamine and uric acid, *Sens. Actuators, B*, 2016, **227**, 488–496, DOI: **10.1016/j.snb.2015.12.073**.

57 M. M. Rahman, A. A. Mamun, H. Minami, M. M. Rahman, S. M. Hoque and H. Ahmad, Biochar/poly(aniline-pyrrole) modified graphite electrode and electrochemical behavior for application in low-cost supercapacitor, *Arabian J. Chem.*, 2024, **17**(9), 105938, DOI: **10.1016/j.arabjc.2024.105938**.

58 H. Gao, F. Wu, X. Wang, C. Hao and C. Ge, Preparation of $NiMoO_4$-PANI core-shell nanocomposite for the high-performance all-solid-state asymmetric supercapacitor, *Int. J. Hydrogen Energy*, 2018, **43**(39), 18349–18362, DOI: **10.1016/j.ijhydene.2018.08.018**.

59 M. Esmaeili, M. M. Abdi, A. P. Mathew, M. Jonoobi, K. Oksman and M. Rezayi, Synergy effect of nanocrystalline cellulose for the biosensing detection of glucose, *Sensors*, 2015, **15**(10), 24681–24697, DOI: **10.3390/s151024681**.

60 M. L. M. Napi, S. M. Sultan, R. Ismail, K. W. How and M. K. Ahmad, Electrochemical-based biosensors on different zinc oxide nanostructures: A review, *Materials*, 2019, **12**(18), 2985, DOI: **10.3390/ma12182985**.

61 X. Liu, M. Li, J. Zheng, X. Zhang, J. Zeng, Y. Liao, J. Chen, J. Yang, X. Zheng and N. Hu, Electrochemical detection of

ascorbic acid in finger-actuated microfluidic chip, *Micromachines*, 2022, **13**(9), 1479, DOI: **10.3390/mi13091479**.

62 Y. Pan, J. Zuo, Z. Hou, Y. Huang and C. Huang, Preparation of electrochemical sensor based on zinc oxide nanoparticles for simultaneous determination of AA, DA, and UA, *Front. Chem.*, 2020, **8**, 592538, DOI: **10.3389/fchem.2020.592538**.

63 G. Darabdhara, B. Sharma, M. R. Das, R. Boukherroub and S. Szunerits, Cu-Ag bimetallic nanoparticles on reduced graphene oxide nanosheets as peroxidase mimic for glucose and ascorbic acid detection, *Sens. Actuators, B*, 2017, **238**, 842–851, DOI: **10.1016/j.snb.2016.07.106**.

64 M. Doulache, M. Trari and B. Saidat, Bimetallic CoPt nanoparticles-modified Pt disk electrode for the amperometric sensing of ascorbic acid, *J. Chem. Sci.*, 2018, **130**(8), 110, DOI: **10.1007/s12039-018-1513-5**.

65 S. A. Hashemi, S. M. Mousavi, S. Bahrani, S. Ramakrishna, A. Babapoor and W.-H. Chiang, Coupled graphene oxide with hybrid metallic nanoparticles as potential electrochemical biosensors for precise detection of ascorbic acid within blood, *Anal. Chim. Acta*, 2020, **1107**, 183–192, DOI: **10.1016/j.aca.2020.02.018**.

66 B. Yan, Y. Yang, Y. Xie, J. Li and K. Li, Fe doping enhances the peroxidase-like activity of CuO for ascorbic acid sensing, *Chemistry*, 2023, **5**(2), 1302–1316, DOI: **10.3390/chemistry5020088**.

67 L. T. Tran, H. V. Tran, C. D. Huynh, C. D. Sai and N. T. Duong, Iron/Iron(III) Oxide decorated on electrochemically reduced graphene oxide: A novel one-step electrosynthesis and a fabrication of an electrochemical ascorbic acid sensor, *J. Electrochem. Soc.*, 2024, **171**(3), 037525, DOI: **10.1149/1945-7111/ad3395**.

68 F. Parkook, S. K. Shahvandi, M. Ghaedi, H. Javadian and A. Parkook, Determination of ascorbic acid in biological samples using an electrochemical sensor modified with Au-Cu_2O/MWCNTs nanocomposite, *Diamond Relat. Mater.*, 2024, **144**, 110954, DOI: **10.1016/j.diamond.2024.110954**.

69 R. Shanmugam, S. Aniruthan, V. Yamunadevi, S. Nellaiappan, A. J. Amali and D. Suresh, Co-N/Zn@NPC derived from bimetallic zeolitic imidazolate frameworks: A dual mode simultaneous electrochemical sensor for uric acid and ascorbic acid, *Surf. Interfaces*, 2023, **40**, 103103, DOI: **10.1016/j.surfin.2023.103103**.